

Microclimate-Interactive Energy Management of Building Clusters: Linking Local Meteorology Effect with Terminal Operation Efficiency

Zhenwei Zhang, *Graduate Student Member, IEEE*, Hongxun Hui, *Senior Member, IEEE, Senior Member, CSEE* and Yonghua Song, *Fellow, IEEE, Fellow, CSEE*

Abstract—Building clusters are primary entities in urban power systems, where terminal energy facilities, including photovoltaic-thermal systems (PV/T) and air conditioners (ACs), are widely deployed to meet diverse user demands. However, the operational efficiency of above facilities and user demands are highly sensitive to meteorological factors, particularly the microscale temperature distribution surrounding buildings. In turn, building clusters significantly reshape local microclimate conditions through waste heat emissions and surface morphology. To capture this interaction and improve operational efficiency, this paper proposes a microclimate-interactive energy management framework for building clusters, which links urban-scale microclimate formation to terminal-level energy dynamics. First, an urban microclimate model is developed that incorporates building emissions and decomposes the spatial domain into four layers. Then, refined models for PV/T and ACs are proposed to characterize temperature-dependent efficiency under varying microclimate conditions. Furthermore, to address user demand uncertainty and its correlation with the surrounding microclimate, a distributionally robust chance-constrained optimization model based on the Wasserstein-metric ambiguity set is developed to obtain the trade-off between operational robustness and economic performance. Case studies demonstrate that the proposed model effectively captures hierarchical feedback between building clusters and surrounding microclimate, and enhances the robustness and adaptability of terminal-level energy operation under dynamic environmental conditions.

Index Terms—Building clusters, air conditioners, photovoltaic and thermal systems, urban microclimate, distributionally robust chance-constrained optimization.

I. INTRODUCTION

THE building clusters serve as the primary entities for energy-related activities in urban areas. In terms of energy consumption, operational demands (specifically for space cooling/heating, hot water, and lighting) account for 30% of global final energy consumption and 26% of global energy-related emissions [1]. Regarding energy generation, rooftop photovoltaic (PV) has shown considerable potential in urban building clusters, which will meet 25% to 49% of global

This paper is funded in part by the China Southern Power Grid Company Limited (GDKJXM20231411), in part by the Guangdong Basic and Applied Basic Research Foundation, China (2025A1515011531), in part by the National Natural Science Foundation of China (Grant No. 52407075), in part by the Science and Technology Development Fund, Macau SAR (File no. 001/2024/SKL), and in part by the Chair Professor Research Grant of University of Macau (File no. CPG2024-00015-IOTSC). (Corresponding author: Yonghua Song.)

Z. Zhang, H. Hui and Y. Song are with the State Key Laboratory of Internet of Things for Smart City and Department of Electrical and Computer Engineering, University of Macau, Macao, China.

electricity demand by 2050 [2]. In recent years, significant attention has been devoted to building energy system optimization and various effective strategies have been proposed for energy saving [3], energy-efficient technologies [4], peak-valley regulation [5], and carbon emission reduction [6]. However, there are still two issues requiring further attention:

(i) *Dynamic Characteristics of Energy Facilities*: Most existing research assumes that energy facilities operate under ideal or rated conditions, leading to overly optimistic optimization solutions. In reality, deteriorating operating conditions and overloaded user demands can cause energy facilities to deviate from optimal efficiency points. Specifically, PV [7] and temperature-controlled units (e.g., ACs) [8] are highly sensitive to meteorological parameters. As ambient temperature increases, the heat generated by PV cells and AC condensers becomes harder to dissipate, resulting in reduced operational efficiency. In extreme cases, excessively high ambient temperatures can even cause these units to shut down [9].

(ii) *Interaction with Surrounding Microclimate*: Most existing research relies on macroscale meteorological forecasts or observations from weather stations as external input [10]. However, the macroscale meteorological model, based on satellite data, operates at spatial scales exceeding 100 km, making it inadequate for capturing neighborhood-level variations. Furthermore, weather stations, typically located in open spaces, tend to underestimate temperature increases within building clusters [11]. In contrast, urban microclimate, localized surrounding buildings with a scale of 1 km, directly impacts energy facilities and user demands. Moreover, the microclimate exhibits lower inertia compared to macroscale model, making it more responsive to building activities [12].

With global warming and increasing urbanization, urban microclimate phenomena (e.g., urban heat islands [13]), have garnered widespread attention. On clear days, the scarcity of green spaces, heat reflection from man-made surfaces, wind resistance of buildings, and anthropogenic heat accumulation lead to significant heat accumulation and temperature rise [14]. In certain urban areas, driven by microclimate phenomena, the temperature rise around the building clusters can exceed 2.5°C, leading to an additional 15% increase in energy consumption density compared to the reference rural areas [15]. Therefore, microscale meteorological analysis for building clusters is a critical prerequisite for accurately modeling building energy activities. Several studies have developed numerical models based on the urban thermal model to simulate the microclimate temperature distribution [16]. The urban thermal

model divides the space surrounding buildings into the urban boundary layer, the urban canopy layer, and the urban surface layer [17], [18]. Furthermore, many researchers have focused on the impact of building operation on localized urban weather. Miguel et al. [19] coupled the EnergyPlus with a lumped thermal parameter model to estimate the temperature and specific humidity in the near-surface urban environment. Duan et al. [20] presented a lumped urban-building thermal coupling model which captures the fundamental physical mechanism for thermal interactions between buildings and their urban environment. However, the studies mentioned above primarily focus on the role of energy system operations in influencing the microclimate, while neglecting the feedback effect of changes in microscale meteorological conditions on the building energy facilities and load demands.

Decentralized solar facilities are critical energy sources and a promising path toward carbon neutrality for building clusters. Existing systems can be categorized based on installation methods (rooftop and facade types) and operational principles (photovoltaic, photothermal, and photovoltaic-thermal systems, PV/T). Among these, rooftop PV/T is widely recognized as an ideal solution with higher efficiency and low-cost installation [21]. Currently, most research focuses on module design and static energy efficiency optimization [22]. For instance, high efficiency photovoltaic cells and composite materials with enhanced heat transfer are utilized to improve overall performance [23]. Additionally, novel cooling technologies (e.g., liquid cooling, air cooling) are adopted to reduce PV panel temperatures [24]. Integrated PV/T and energy storage systems are also developed for peak-valley regulation, reducing reliance on external energy sources [25], [26]. However, the above studies primarily focus on the static performance of PV/T and lack the dynamic characterization analysis under realistic varying microscale meteorological conditions.

Air conditioners (ACs) are the primary electricity consumers in building clusters, accounting for more than 70% of the total load during the cooling season [27]. Similar to PV, both operational characteristics and cooling demand are sensitive to meteorological conditions. Currently, model-driven, data-driven, and hybrid data-model-driven approaches have been proposed to establish numerical relationships among cooling loads, external environment, and internal user behavior [28]. However, most studies assume that ACs operate under rated operating conditions with a fixed coefficient of performance (COP) [29]. In reality, COP dynamically varies with both the ambient and indoor temperature through experimental tests [30]. Specifically, when the operating temperature of condensers becomes too high, the compressor requires more power to maintain effective heat exchange [31]. Simultaneously, the elevated condenser temperature diminishes the system's cooling capacity, significantly reducing the COP. Under the microclimate effects, condensers are subjected to harsher operating conditions.

Energy demands of building clusters are influenced by indoor traffic and user behaviors, resulting in high levels of uncertainty and random fluctuations [32]. To address load uncertainty, various optimization methods have been proposed, primarily categorized into stochastic optimization (SO), robust

optimization (RO), and distributionally robust optimization (DRO). SO employs probability distributions to predict loads and make decisions based on expected function [33]. However, it is heavily dependent on the accuracy of the probability distributions and incurs a significant computational burden in practical applications. RO eliminates the need for precise probability distributions by constructing an uncertainty set [34], [35]. However, it often produces overly conservative results since the optimal solution must satisfy all worst-case scenario within the uncertainty set. DRO, which combines the strengths of SO and RO, has gained significant attention [36]. According to the construction method of the uncertainty set, the current DRO methods can be categorized into moment constraint-based and distance metric-based [37]. Among these, the Wasserstein distance-based approach is widely applied in building load optimization due to its robustness against outliers and its capability to capture local variations in distributions [38]. Furthermore, to ensure demands can be met for the majority of operational periods, the distributionally robust chance constraint (DRCC) approach has been introduced [39]. DRCC ensures that optimization solutions satisfy constraints with high probability during actual operation by defining chance constraints over the uncertainty set of distributions.

Above all, the dynamic operating characteristics of energy facilities in building clusters under varying microclimate conditions still exist research gaps, and refined energy management models incorporating load uncertainty still need further analysis. The major contributions of this paper are threefold:

- 1) We propose a microclimate model for urban building clusters that incorporates underlying structures and anthropogenic emissions. This model offers a numerical approach to calculate the temperature distribution across the spaces and surfaces surrounding the building cluster.
- 2) We propose an integrated dynamic efficiency model for energy facilities considering surrounding microclimate interaction. For PV/T, the model quantifies the dynamic heat transfer process and the electrical/thermal output under varying meteorological conditions. For ACs, the model quantifies the dynamic relationship between COP following ambient and indoor temperature, considering refrigerant enthalpy change and heat transfer processes.
- 3) We established a distributionally robust chance-constrained optimization framework based on Wasserstein-metric ambiguity set to address user demand uncertainty. The proposed model is further reformulated as a mixed-integer programming problem and validated in the building clusters of Macao.

We state our problem in Section II. The urban microclimate model is established in Section III. The dynamic energy efficiency model is established in Section IV. The DRCC framework is established in Section V. Numerical experiments are presented in Section VI. Section VII concludes this paper.

II. INTERACTION BETWEEN URBAN MICROCLIMATE AND BUILDING CLUSTERS

This paper studies the microclimate-interactive energy management of building clusters, particularly focusing on terminal-level energy dynamics and user demand under urban-scale

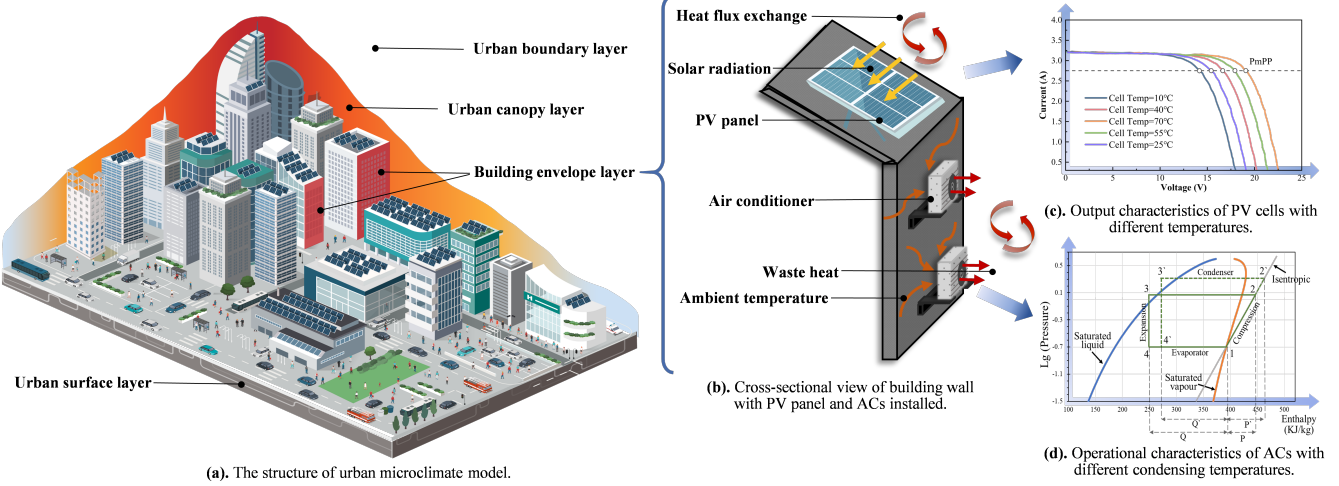


Fig. 1. The dynamic energy efficiency of building clusters under surrounding microclimate interaction.

microclimate feedback. As shown in Fig. 1(a), the proposed microclimate model divides the urban space into boundary layer, canopy layer, surface layer, and building envelope layer. Compared to macroscale and mesoscale models, microclimate model captures neighborhood-level meteorological variations by considering building energy emissions, underlayer structures, wind resistance, and solar reflection. Notably, the urban canopy exhibits a significant temperature gradient that follows the height and density distribution of buildings. Simultaneously, building envelope layers frequently experience considerably higher temperatures than surrounding air due to the thermal inertia of artificial surfaces.

Terminal energy facilities are installed on exterior surfaces, with their operational characteristics directly influenced by surrounding microclimate conditions, depicted in Fig. 1(b). For PV units, the diode characteristics within cells lead to a rapid decline in generation efficiency as temperature raises, as shown in Fig. 1(c). For example, on a clear summer day, a high temperature results in PV cells only at an efficiency of 18% or less. For ACs, the heat transfer process is more significantly influenced by the ambient temperature. ACs transfer heat from indoors to outdoors through compressor-driven refrigerant, with the ideal refrigeration cycle represented as 1-2-3-4-1 in the pressure-enthalpy diagram, as shown in Fig. 1(d). In reality, the actual temperature of the building envelope where the condensing unit is located will be much higher than the ideal operating temperature. At this point, the increase in condensing temperature causes the refrigeration cycle to shift to 1-2'-3'-4'-1. Compared to ideal conditions, ACs consume more power P' at the compressor, but produce less cooling Q' at the evaporator, implying a significant loss in COP. Numerical urban microclimate model and dynamic energy efficiency model of PV/T and ACs are presented below.

III. MICROCLIMATE MODEL FOR BUILDING CLUSTERS

A. Urban Boundary Layer

The urban boundary layer is the initial condition and upper boundary of urban canopy layer, typically encompassing a mesoscale meteorological evolution. In this study, the data of

urban boundary layer is sourced from geostationary operational environmental satellites, specifically from the National Weather Science Data Centre [40].

B. Urban Canopy Layer

The urban canopy layer, situated between urban boundary and surface layers, varies in height with building elevation. The temperature distribution within this layer is significantly influenced by the type of underlying surface, which impacts the transfer and accumulation of heat flux around buildings. For building clusters, urban canopy layer exchanges heat with neighboring layers (e.g., urban boundary layer, urban surface layer, building envelope layer) and absorbs anthropogenic heat emissions, as shown in (1).

$$\begin{aligned} \rho_a c_a V_{uc} \frac{dT_{uc,t}}{dt} &= \rho_a c_a q_{ub,t} (T_{ub,t} - T_{uc,t}) \\ &+ h_{ex,t} A_{sur} (T_{sur,t} - T_{uc,t}) + A_{total} Q_{eh,t} \\ &+ \sum_{k \in \psi_b} \left\{ \rho_a c_a q_{ve,k} (T_{in,k,t} - T_{uc,t}) + Q_{waste,k,t} \right\} \\ &+ h_{ex,t} A_{en,k} (T_{en,k,t} - T_{uc,t}) \end{aligned} \quad (1)$$

where ρ_a and c_a are the density and specific heat capacity of air, respectively; $T_{uc,t}$, $T_{sur,t}$, $T_{in,k,t}$, and $T_{en,k,t}$ are the temperature of urban canopy layer, surface layer, building indoor and building envelope layer, respectively; A_{sur} , A_{total} , and $A_{en,k}$ are the area of urban surface layer, building cluster, and building envelope layer, respectively; V_{uc} is the control volume of urban canopy layer; $q_{ub,t}$ is the airflow rate between urban boundary layer and canopy layer, $q_{ub,t} = [(L_b - x_{0,b})L_b] (1 - \lambda_b) v_t$; L_b and λ_b are the averaging length scale and building density; v_t is the mean wind speed; $x_{0,b}$ is the length scale of order; $q_{ve,k}$ is the ventilation rate between building indoor and urban canopy layer, $q_{ve,t} = ACH_b \times A_{f,b} \times H_b$; ACH_b is the air change time; $A_{f,b}$ is the lateral area of heat exchange between the control volume and its surroundings; H_b is the average building height; $Q_{eh,t}$ and $Q_{waste,k,t}$ are the average anthropogenic heat density and waste heat; $h_{ex,t}$ is the convective heat transfer coefficient, $h_{ex,t} = 5.7 + 3.8v_t$; t , k , and b are the index of time, building,

and building cluster, respectively; ψ_b is the index set of all buildings. The remaining terms of (1) on the right-hand side represent the convective heat from urban boundary layer, the convective heat from urban surface layer, the anthropogenic heat within building cluster, the convective heat from building indoor, the waste heat from air conditioners, and the convective heat from building envelop layer.

C. Urban Surface Layer

The urban surface layer refers to the upper surface to the depth having a constant temperature. Within the building clusters, the urban surface layer absorbs solar heat and exchanges it through ground reflection, vegetation transpiration, and convection with the neighboring layers, as shown in (2).

$$\begin{aligned} \sum \rho_i c_i \Delta x_i A_{sur,i} \frac{dT_{sur,t}}{dt} &= (1 - \gamma_b) A_{sur} I_{sun,t} \\ &+ K_r A_{sur,r} (\bar{T}_{sur,r} - T_{sur,t}) / \Delta x_r - Q_{rad} A_{sur,r} \quad (2) \\ &+ K_v A_{sur,v} (\bar{T}_{sur,v} - T_{sur,t}) / \Delta x_v - Q_{evp} A_{sur,v} \\ &+ h_{ex,t} A_{sur} (T_{uc,t} - T_{sur,t}) \end{aligned}$$

where $\sum \rho_i c_i \Delta x_i A_{sur,i}$ is the sum of the thermal mass of surface layer; i is the index of surface types, including vegetated and man-made underlying surface; ρ_i and c_i are the density and heat capacity of surface i , respectively; Δx_i and $A_{sur,i}$ are the effective depth and area, respectively; γ_b is the albedo; $I_{sun,t}$ is the solar radiation intensity; K_v and K_r are the conductivities of vegetated and man-made surfaces, respectively; $A_{sur,r}$ and $A_{sur,v}$ are the area of vegetated and man-made surfaces, respectively; $\bar{T}_{sur,r}$ and $\bar{T}_{sur,v}$ are the vegetated and man-made underlying temperatures at effective depth, respectively; Δx_v and Δx_r are the effective depth of vegetated and man-made surfaces, respectively; Q_{evp} and Q_{rad} are the transpiration and long-wave radiation heat flux, respectively. The remaining terms of (2) on the right-hand side represent solar radiation heat, the conductive heat from man-made surface, the reflection heat from man-made surface, the conductive heat from vegetative surface, the vegetation transpiration, the convective heat from urban canopy layer.

D. Building Envelop Layer

The building envelope layer refers to the control volume from the exterior to interior surface of buildings. The accumulation of solar heat flux in man-made surfaces causes its temperature to be significantly higher than the surrounding air temperature. The heat transfer process is described as (3).

$$\begin{aligned} \rho_{en} c_{en} V_{en,k} \frac{dT_{en,k,t}}{dt} &= (1 - \alpha_k) \lambda_k A_{en,k} I_{sun,t} \\ &+ h_{ex,t} A_{en,k} (T_{uc,t} - T_{en,k,t}) \quad (3) \\ &+ h_{ei,k} A_{en,k} (T_{in,k,t} - T_{en,k,t}) \end{aligned}$$

where ρ_{en} and c_{en} are the density and specific heat capacity of the building envelope, respectively; $V_{en,k}$ is the control volume; α_k is albedo of the building envelope; λ_k is the percentage of effective sunlit area of the building envelop; $h_{ei,k}$ is heat transfer coefficient between building indoor air and building envelope layer. The remaining terms of (3) on

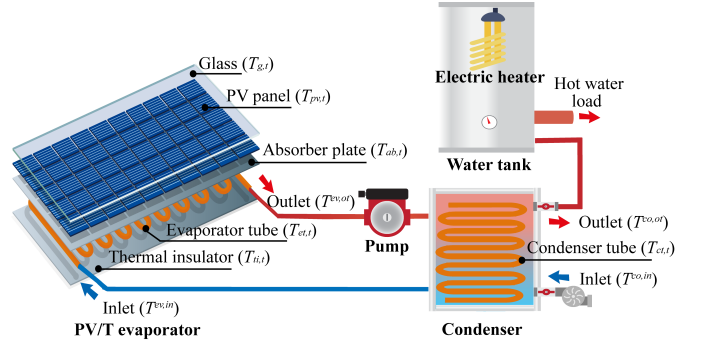


Fig. 2. The structure of photovoltaic/thermal system.

the right-hand side represent solar radiation heat, the convective heat from urban canopy layer, the convective heat from building indoor air.

IV. DYNAMIC ENERGY EFFICIENCY MODEL CONSIDERING MICROCLIMATE CONDITIONS

A. Photovoltaic/Thermal System

An integrated photovoltaic thermal system (PV/T) is described in this section, with its main components comprising an evaporator, condenser, electric heater, and water tank, as shown in Fig. 2. Under clear weather conditions, the PV/T evaporator absorbs solar radiation to generate electricity while heating the working fluid. The cooling water is heated in the condenser and injected into water tank to meet the load requirements, supplemented by the electric heater. The numerical models for each component are established below.

1) PV/T Evaporator: Unlike a single PV panel, the PV/T evaporator uses a heat-absorbing mass cycle for heat recovery, preventing excessive panel temperatures and enhancing power generation efficiency. The heat transfer process involves several key components: the glass plate, PV panel, heat absorber plate, evaporator tube, and thermal insulator, as shown below:

Heat flux balance in glass:

$$m_g c_g \frac{dT_{g,t}}{dt} = I_{sun,t} \alpha_g A_g + h_{g-a,t} A_g (T_{uc,t} - T_{g,t}) \quad (4)$$

$$+ h_{g-pv,t} A_g (T_{pv,t} - T_{g,t}) + Q_{g-pv,t} - Q_{g-a,t}$$

$$Q_{g-pv,t} = \frac{\sigma A_g (T_{pv,t}^4 - T_{g,t}^4)}{1/\varepsilon_g + 1/\varepsilon_{pv} - 1} \quad (5)$$

$$Q_{g-a,t} = \varepsilon_g \sigma A_g (T_{g,t}^4 - T_{uc,t}^4) \quad (6)$$

where g , a , and pv are the index of Glass, ambient air, and PV panel, respectively; m , c , T , A , α , and ε are the mass, specific heat capacity, temperature, area, absorptivity, and emissivity, respectively; $h_{g-a,t}$ is the convective heat transfer coefficients between glass and ambient air, $h_{g-a,t} = 2.8 + 3.0 v_t$; $h_{g-pv,t}$ is the convective heat transfer coefficients between glass and PV panel, $h_{g-pv,t} = Nu \cdot k_a / l_{g-pv}$; Nu and σ are the Nusselt number and Stefan-Boltzmann constant; k_a is heat conductivity coefficient of air; l_{g-pv} is the thickness of the air gap between glass and PV panel; $Q_{g,pv}$ and $Q_{g,a}$ are the radiative heat transfer between the PV panel and glass, glass and ambient air, respectively. The right-hand side of (4)

represents the solar radiation absorbed, the heat conduction between the glass and urban canopy layer, the heat conduction between the glass and PV panel, the radiative heat transfer between glass layer and surrounding ambient air.

Heat flux balance in PV panel:

$$\begin{aligned} m_{pv}c_{pv}\frac{dT_{pv,t}}{dt} &= I_{sun,t}\alpha_{pv}A_{pv} - E_{pv,t} \\ &+ h_{g-pv,t}A_{pv}(T_{g,t} - T_{pv,t}) - Q_{g-pv,t} \quad (7) \\ &+ h_{pv-ab,t}A_{pv}(T_{ab,t} - T_{pv,t}) - Q_{pv-ab,t} \end{aligned}$$

$$E_{pv} = I_{sun,t}A_{pv}\tau\eta_{ref}[1 - \beta_{pv}(T_{pv,t} - T_{ref})] \quad (8)$$

$$Q_{pv-ab,t} = \frac{\sigma A_{pv}(T_{pv,t}^4 - T_{ab,t}^4)}{1/\varepsilon_{pv} + 1/\varepsilon_{ab} - 1} \quad (9)$$

where ab is the index of the absorber plate; E_{pv} in (8) is the power generation of PV panel; $h_{pv-ab,t}$ is the convective heat transfer coefficients between PV panel and absorber plate, $h_{pv-ab,t} = Nu \cdot k_a/l_{pv-ab}$; l_{pv-ab} is the thickness of the air gap between PV panel and absorber plate; $Q_{pv-ab,t}$ in (9) is the radiative heat transfer between the PV panel and absorber plate; τ is the transmittance of PV panel; η_{ref} is the referenced electrical efficiency with a cell temperature of 298K; β_{pv} is the temperature coefficient. The right-hand side of (7) represents the solar radiation absorbed, power generation of PV panel, the heat conduction and radiative heat transfer between the PV panel and glass layer, the heat conduction and radiative heat transfer between the PV panel and absorber plate.

Heat flux balance in absorber plate:

$$\begin{aligned} m_{ab}c_{ab}\frac{dT_{ab,t}}{dt} &= h_{pv-ab,t}A_{ab}(T_{pv,t} - T_{ab,t}) + Q_{pv-ab,t} \\ &+ h_{ab-et}A_{ab}(T_{et,t} - T_{ab,t}) + h_{ab-ti}A_{ab}(T_{ti,t} - T_{ab,t}) \quad (10) \end{aligned}$$

where et and ti are the index of the evaporator tube and thermal insulator, respectively; h_{ab-et} is the convective heat transfer coefficients between absorber plate and evaporator tube, $h_{ab-et} = \frac{d_{ab}L_{ab}}{A_{ab}} \cdot \frac{8\lambda_{ab}}{W_{et}-D_{et}}$; d_{ab} , L_{ab} , and λ_{ab} are the thickness, length, and heat conductivity coefficient of absorber plate, respectively; W_{et} and D_{et} are the tube pitch and external diameter of evaporator tube, respectively. The right-hand side of (10) represents the heat conduction and radiative heat transfer between the PV panel and absorber plate, the heat conduction between absorber plate and evaporator tube, the heat conduction between absorber plate and thermal insulator.

Heat flux balance in evaporator tube:

$$\begin{aligned} m_{et}c_{et}\frac{dT_{et,t}}{dt} &= h_{ab-et}A_{et}(T_{ab,t} - T_{et,t}) \\ &+ h_{et-ti}A_{et}(T_{ti,t} - T_{et,t}) - h_{et-w}\pi d_{et}L_{et}(T_{et,t} - T_{r,t}^{ev}) \quad (11) \end{aligned}$$

where r is the index of refrigerant; h_{et-ti} and h_{et-w} are the convective heat transfer coefficients between evaporator tube and thermal insulator, coefficients between evaporator tube and refrigerant, respectively; d_{et} and L_{et} are the diameter and length of evaporator tube, respectively; T_r^{ev} is the average temperature of refrigerant in the evaporator. The right-hand side of (11) represents the heat conduction between the absorber plate and evaporator tube, the heat conduction between the thermal

insulator and evaporator tube, and the heat conduction between the evaporator tube and refrigerant.

Heat flux balance in thermal insulator:

$$\begin{aligned} m_{ti}c_{ti}\frac{dT_{ti,t}}{dt} &= h_{et-ti}A_{et}(T_{et,t} - T_{ti,t}) \\ &+ h_{ti-a}A_{ti}(T_{uc,t} - T_{ti,t}) + h_{ab-ti}A_{ab}(T_{ab,t} - T_{ti,t}) \quad (12) \end{aligned}$$

The right-hand side of (12) represents the heat conduction between the evaporator tube and thermal insulator, the heat conduction between the surrounding ambient air and thermal insulator, the heat conduction between the absorber plate and thermal insulator.

2) Refrigerant Cycle: Considering the conservation of energy at a steady state, the refrigerant absorbs the energy supplied by the evaporator and compressor and then transfers it to the cooling water through the condenser. The heat flux balance can be described below.

$$\begin{aligned} m_r c_r \frac{dT_{r,t}^{ev}}{dt} &= h_{et-r}\pi d_{et}L_{et}(T_{et,t} - T_{r,t}^{ev}) \\ &+ m_r c_r (T_{r,t}^{ev,in} - T_{r,t}^{ev,out}) \quad (13) \end{aligned}$$

$$\begin{aligned} m_r c_r \frac{dT_{r,t}^{co}}{dt} &= h_{ct-r}\pi d_{ct,t}L_{ct}(T_{ct,t} - T_{r,t}^{co}) \\ &+ m_r c_r (T_{r,t}^{co,in} - T_{r,t}^{co,out}) \quad (14) \end{aligned}$$

where co and ct are the index of condenser and condenser tube, respectively; $T_{r,t}^{ev,in}$ and $T_{r,t}^{ev,out}$ are the inlet and outlet temperature of refrigerants in evaporator, respectively; $T_{r,t}^{co,in}$ and $T_{r,t}^{co,out}$ are the inlet and outlet temperature of refrigerants in condenser, respectively; neglecting pipe friction and heat loss, $T_{r,t}^{ev,out} = T_{r,t}^{co,in}$, $T_{r,t}^{co,out} = T_{r,t}^{ev,in}$; d_{ct} and L_{ct} are the diameter and length of condenser tube, respectively.

3) Condenser: The twisted condenser tubes ensure sufficient heat exchange between the refrigerant and the cooling water. Considering the steady state case, the heat flux balance in the condenser can be described below:

$$\begin{aligned} m_{ct}c_{ct}\frac{dT_{ct,t}}{dt} &= h_{ct-w}\pi d_{ct}L_{ct}(T_{w,t}^{co} - T_{ct,t}) \\ &+ h_{ct-r}\pi d_{ct}L_{ct}(T_{r,t}^{co} - T_{ct,t}) \quad (15) \end{aligned}$$

$$\begin{aligned} m_w c_w \frac{dT_{w,t}^{co}}{dt} &= h_{ct-w}\pi d_{ct}L_{ct}(T_{ct,t} - T_{w,t}^{co}) \\ &+ m_w c_w (T_{w,t}^{co,in} - T_{w,t}^{co,out}) \quad (16) \end{aligned}$$

$$H_{pv,t} = m_w c_w (T_{w,t}^{co,in} - T_{w,t}^{co,out}) \quad (17)$$

where w is the index of cooling water; $T_{w,t}^{co,in}$ and $T_{w,t}^{co,out}$ are the temperature of cooling water in the inlet and outlet of the condenser; H_{pv} is the heat generation of PV/T.

4) Electric Heater: The electric heater assists PV/T in meeting hot water demand, typically with a fixed thermal conversion efficiency, which can be expressed as:

$$H_{eh,t} = \eta_{eh} \cdot P_{eh,t} \quad (18)$$

where $H_{eh,t}$, $P_{eh,t}$, and η_{eh} are heat output, power consumption, and conversion efficiency of electric heater, respectively.

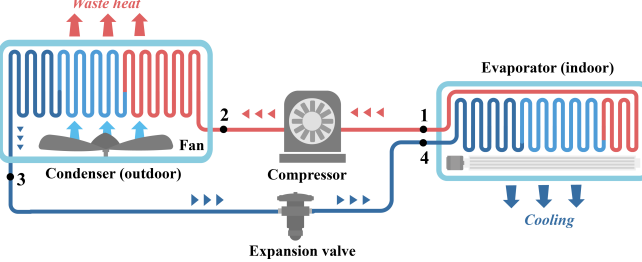


Fig. 3. The structure of an air-cooled air conditioning system.

5) *Water Tank*: The water tank enables intertemporal heat transfer of PV/T, working with electric heaters to balance peak-valley fluctuations in heat loads. The heat capacity balance in water tank can be described as:

$$E_{hs,t+1} = (1 - \tau_{hs}) E_{hs,t} + [\eta_{hs}^{ch} H_{hs,t}^{ch} - H_{hs,t}^{dis}/\eta_{hs}^{dis}] \Delta t \quad (19)$$

where $E_{hs,t+1}$ is the heat capacity of water tank at time $t+1$; τ_{hs} is the self-loss coefficient; η_{hs}^{ch} and η_{hs}^{dis} are the heat charge and discharge efficiency, respectively; $H_{hs,t}^{ch}$ and $H_{hs,t}^{dis}$ are the heat charge and discharge power, respectively.

B. Air Conditioners

An air-cooled air conditioning system is described in this section, as depicted in Fig. 3. The system operates by circulating refrigerant to facilitate efficient heat absorption and release. During the refrigeration cycle, the refrigerant undergoes continuous phase transitions (e.g., gas, liquid, or gas-liquid mixture), making its internal energy variations challenging to quantify using conventional temperature-based heat transfer models. In this paper, an energy-efficiency calculation model is proposed, integrating enthalpy dynamics with heat transfer principles. The detailed numerical formulations are as follows:

1) *Energy Balance in Compressor*: The compressor converts mechanical energy into the internal energy of the refrigerant, causing it to transition from a low-temperature, low-pressure gas to a high-temperature, high-pressure gas. Neglecting friction and heat loss, the work performed by the compressor is described as an isentropic process. The temperature and pressure variations of the refrigerant at the compressor inlet and outlet are governed by (20), while the compressor's power consumption is defined in (21).

$$\left(\frac{p_{2,t}}{p_{1,t}}\right)^{\frac{\gamma-1}{\gamma}} = \left(\frac{T_{2,t}}{T_{1,t}}\right) \Leftrightarrow T_{2,t} = T_{1,t} \left(\frac{p_{2,t}}{p_{1,t}}\right)^{\frac{1}{\gamma}} \quad (20)$$

$$P_{com,t} = \dot{m} \cdot R \cdot T_{1,t} \cdot \ln \left(\frac{p_{2,t}}{p_{1,t}}\right) \quad (21)$$

where γ is the specific heat ratio of refrigerant; $p_{1,t}$ and $p_{2,t}$ are the inlet and outlet pressure of compressor, respectively; $T_{1,t}$ and $T_{2,t}$ are the inlet and outlet temperature of compressor, respectively; $P_{com,t}$ is the compressor power; \dot{m} and R are the mass flow and gas constant, respectively. Neglecting pipe friction and heat loss, $p_{2,t}$ and $T_{2,t}$ are also inlet pressure and temperature of condenser, respectively; $p_{1,t}$ and $T_{1,t}$ are also outlet pressure and temperature of evaporator, respectively.

2) *Energy Balance in Condenser*: Assuming negligible friction, the heat exchange in condenser is treated as isobaric, as shown in (22). Driven by the fan, the refrigerant exchanges heat fully with the ambient air, reaching thermal equilibrium. Considering microclimate effects, the operating temperature of condenser installed on the wall surface is approximated as the building envelope layer temperature, as shown in (23).

$$p_{3,t} = p_{2,t} \quad (22)$$

$$T_{3,t} = T_{en,t} \quad (23)$$

where $p_{3,t}$ and $T_{3,t}$ are the outlet pressure and temperature of condenser, respectively. Neglecting pipe friction and heat loss, $p_{3,t}$ and $T_{3,t}$ are also the inlet pressure and temperature of expansion value, respectively.

As condenser operating temperature rises, the compressor needs to increase outlet pressure to elevate the refrigerant vaporization temperature. A specific degree of subcooling ΔT_{co} is generally applied to ensure complete liquefaction of the refrigerant at the condenser outlet. Based on the outlet temperature setting, the outlet pressure can be calculated by (24). Using the temperature and pressure, the refrigerant's enthalpy in condenser can be determined by (25) and (26).

$$p_{3,t} \propto f [p : (T_{3,t} + \Delta T_{co}), Q = 0, \text{R134a}] \quad (24)$$

$$h_{2,t} \propto f [h : p_{2,t}, T_{2,t}, \text{R134a}] \quad (25)$$

$$h_{3,t} \propto f [h : p_{3,t}, T_{3,t}, \text{R134a}] \quad (26)$$

where $f [\cdot]$ is state function; Q is the status flag of refrigerant, $Q = 0$ refers to refrigerant in liquid state and $Q = 1$ refers to refrigerant in gas state; R134a is the refrigerant type.

In the condenser, while temperature variation is minimal during the gas-to-liquid phase transition, a substantial amount of latent heat is released into the surrounding air. The waste heat from the condenser can be calculated from the refrigerant's inlet and outlet enthalpy differences, as shown in (27). Additionally, the fan power is adjusted approximately linearly with the condensing temperature, as shown in (28).

$$Q_{waste,t} = \dot{m} (h_{3,t} - h_{2,t}) \quad (27)$$

$$P_{fan,t} = P_{fan,t}^{base} + (T_{3,t} - T_{fan}^{base}) \cdot k_{fan} \quad (28)$$

where $Q_{waste,t}$ is the waste heat emitted by air conditioner; $P_{fan,t}$ is the power of fan; T_{fan}^{base} is the baseline reference temperature; k_{fan} is the adjustment rate.

3) *Energy Balance in Expansion Value*: Assuming an ideal adiabatic process within the expansion valve, the enthalpy remains constant between the inlet and outlet, as shown in (29). Simultaneously, the pressure ratio varies according to the adjustments made by the compressor, as shown in (30). Based on pressure and enthalpy of refrigerant, the temperature can be obtained in (31).

$$h_{3,t} = h_{4,t} \quad (29)$$

$$(p_{2,t}/p_{1,t}) = (p_{3,t}/p_{4,t}) \quad (30)$$

$$T_{4,t} \propto f [T : h_{4,t}, p_{4,t}, \text{R134a}] \quad (31)$$

where $T_{4,t}$, $p_{4,t}$, and $h_{4,t}$ are the temperature, pressure, and enthalpy of refrigerant in the expansion valve outlet, respectively. Neglecting pipe friction and heat loss, $p_{4,t}$ and $T_{4,t}$ are also the inlet pressure and temperature of evaporator, respectively.

4) *Energy Balance in Evaporator:* The refrigerant flows through the evaporator to absorb the indoor heat and change from liquid to gas. Similar to condenser, the heat exchange is isobaric process, as shown in (32). To ensure the refrigerant is fully vaporized, a specific level of superheat ΔT_{ev} is typically maintained at the evaporator outlet, as shown in (33) and (34). The cooling capacity can be obtained from the enthalpy difference between inlet and outlet, as shown in (35) and (36).

$$p_{1,t} = p_{4,t} \quad (32)$$

$$T_{1,t} = T_{in,t} \quad (33)$$

$$p_{4,t} \propto f [p : (T_{1,t} - \Delta T_{ev}), Q = 1, \text{R134a}] \quad (34)$$

$$h_{1,t} \propto f [h : p_{1,t}, T_{1,t}, \text{R134a}] \quad (35)$$

$$Q_{cool,t} = \dot{m} (h_{4,t} - h_{1,t}) \quad (36)$$

where $p_{1,t}$, $T_{1,t}$, and $h_{1,t}$ are the outlet pressure, temperature, and enthalpy of evaporator, respectively.

C. Integrated Energy Efficiency

Energy efficiency is the ratio of output energy to input energy. For the PV/T, the input is sun radiation and the outputs include electricity generated by the PV plant and hot water. The energy efficiency of PV/T is shown in (37). For the ACs, the input consists of the electrical power consumed by the compressor and fan, and the output is the amount of cooling capacity. The energy efficiency of ACs is shown in (38).

$$\eta_{pv} = \frac{\sum_{NT} (H_{pv,t} + E_{pv,t})}{\sum_{NT} I_{sun,t}} \times 100\% \quad (37)$$

$$\eta_{ac} = \frac{\sum_{NT} Q_{cool,t}}{\sum_{NT} (P_{com,t} + P_{fan,t})} \times 100\% \quad (38)$$

V. DISTRIBUTIONAL ROBUST CHANCE CONSTRAINED MODEL CONSIDERING DEMAND UNCERTAINTY

In this section, a DRCC-based optimal dispatch model for building clusters is established considering the user-demand uncertainty. We first introduce the model for electric, cooling, and hot water loads. Then, we describe the formulation of the DRCC problem. Finally, we introduce how to reformulate the proposed model into a tractable problem.

A. User-Demand Model

1) *Electric and Hot Water Load Uncertainty:* The electricity and hot water demands of buildings exhibit significant random fluctuations, closely following the indoor activities of occupants. The uncertainty electric load $\tilde{P}_{load,k,t}$ and hot water load $\tilde{H}_{load,k,t}$ of building k can be expressed as:

$$\tilde{P}_{load,k,t} = \hat{P}_{load,k,t} + \xi_{e,k,t}, \quad (39)$$

$$\tilde{H}_{load,k,t} = \hat{H}_{load,k,t} + \xi_{h,k,t}, \quad (40)$$

where $\hat{P}_{load,k,t}$ and $\hat{H}_{load,k,t}$ are the forecast value of electric and hot water load, respectively; $\xi_{e,k,t}$ and $\xi_{h,k,t}$ are the forecast deviation of electric and hot water load, respectively.

Here, we construct a Wasserstein metric-based ambiguity set \mathcal{P}_W for uncertainty forecast deviation. The ambiguity set defines a ball incorporating all distributions \mathbb{P} that are sufficiently close to the empirical distribution $\hat{\mathbb{P}}$ with respect to the radius θ [41]:

$$\mathcal{P}_W = \left\{ \mathbb{P} \in \mathcal{D}(\Xi) : d_W (\mathbb{P}, \hat{\mathbb{P}}_N) \leq \theta \right\} \quad (41)$$

where $\mathcal{D}(\Xi)$ is the support space; $\hat{\mathbb{P}}_N$ is the reference distribution estimated from the available historical data samples, $\hat{\mathbb{P}}_N = \frac{1}{N} \sum_i^N \delta_{(\xi'_1, \xi'_2, \dots, \xi'_N)}$; N is the number of available historical data samples; δ is the Dirac distribution center of sample; d_W is the Wasserstein distance, defined in (42).

$$\begin{aligned} d_W (\mathbb{P}_1, \mathbb{P}_2) &= \inf_{\Pi \in m(\Xi \times \Xi)} \mathbb{E}_{(\xi_1, \xi_2) \sim \Pi} [\|\xi_1 - \xi_2\|_p] \\ &= \inf_{\Pi \in m(\Xi \times \Xi)} \int d(\xi_1, \xi_2) \Pi(d\xi_1, d\xi_2) \end{aligned} \quad (42)$$

where Π is the joint probability distribution of random variables ξ_1 and ξ_2 with marginals \mathbb{P}_1 and \mathbb{P}_2 ; $\|\cdot\|_p$ represents an arbitrary norm on \mathbb{R}^m ; $p = 1$ and $p = 2$ is the Manhattan distance and Euclidean distance, respectively.

2) *Cooling Load:* Compared with the electric and hot water load, the cooling load is more directly determined by meteorological conditions. Here, the cooling load model based on the first-order heat transfer principle is established in (43).

$$\begin{aligned} \rho_a c_a V_{in,k} \frac{dT_{in,k,t}}{dt} &= h_{ei,k} A_{en,k} (T_{en,k,t} - T_{in,k,t}) \\ &+ \rho_a c_a q_{ve,k,t} (T_{uc,t} - T_{in,k,t}) - Q_{cool,k,t} \\ &+ \beta_k A_{win,k} I_{sun,t} + N_{fl,k} A_{in,k} Q_{ih,k,t} \end{aligned} \quad (43)$$

where V_{in}^{in} is indoor control volume; β_k is sunlight transmission coefficient; $A_{win,k}$ is window area; $N_{fl,k}$ is number of floors; $Q_{ih,k,t}$ is indoor anthropogenic heat density.

B. DRCC-Based Optimiztion Model

1) *Objective Function:* The objective function is to minimize the total operational cost for all buildings:

$$\min_x \sum_t^{NT} C_e P_{main,t} \quad (44)$$

where x is decision variables, $x = [P_{main,t}, P_{ac,k,t}, H_{el,k,t}, H_{hs,k,t}^{ch}, H_{hs,k,t}^{dis}]$; $P_{main,t}$ is the main grid power; $P_{ac,k,t}$ is the ACs power, $P_{ac,k,t} = P_{com,k,t} + P_{fan,k,t}$; C_e is the price.

2) *Unit Constraints:* The electric load forecast deviation is offset by the main grid, while the heat load deviation of each building is managed through cooperation between the water tank and electric heater:

$$\tilde{H}_{eh,k,t} = \hat{H}_{eh,k,t} + \alpha_{eh,k,t} \xi_{h,k,t} \quad (45)$$

$$\tilde{P}_{main,t} = \hat{P}_{main,t} + \sum_{k \in \varphi_b} [\xi_{e,k,t} + \alpha_{k,t} \xi_{h,k,t} / \eta_{eh,k}] \quad (46)$$

$$\tilde{H}_{hs,k,t}^{ch} = \hat{H}_{hs,k,t}^{ch} - \beta_{hs,k,t}^{ch} \xi_{hs,k,t} \quad (47)$$

$$\tilde{H}_{hs,k,t}^{dis} = \hat{H}_{hs,k,t}^{dis} + \beta_{hs,k,t}^{dis} \xi_{hs,k,t} \quad (48)$$

$$\alpha_{eh,k,t} + \beta_{hs,k,t}^{ch} + \beta_{hs,k,t}^{dis} = 1 \quad (49)$$

where $\alpha_{eh,k,t}$, $\beta_{hs,k,t}^{ch}$ and $\beta_{hs,k,t}^{dis}$ are the participation factors.

The chance constraints of units with uncertain output under the uncertainty set are as follows:

$$\inf_{\mathbb{P} \in \mathcal{D}} \mathbb{P} (\tilde{P}_{\text{main},t} \leq P_{\text{main}}^{\max}) \geq 1 - \varepsilon_{\text{main},t} \quad (50)$$

$$\inf_{\mathbb{P} \in \mathcal{D}} \mathbb{P} (\tilde{P}_{eh,k,t} \leq P_{eh,k}^{\max}) \geq 1 - \varepsilon_{eh,t} \quad (51)$$

$$\inf_{\mathbb{P} \in \mathcal{D}} \mathbb{P} (H_{hs,k}^{ch,\min} \leq \tilde{H}_{hs,k,t}^{ch} \leq H_{hs,k,t}^{ch,\max}) \geq 1 - \varepsilon_{hs,t}^{ch} \quad (52)$$

$$\inf_{\mathbb{P} \in \mathcal{D}} \mathbb{P} (H_{hs,k}^{dis,\min} \leq \tilde{H}_{hs,k,t}^{dis} \leq H_{hs,k,t}^{dis,\max}) \geq 1 - \varepsilon_{hs,t}^{dis} \quad (53)$$

$$\inf_{\mathbb{P} \in \mathcal{D}} \mathbb{P} (E_{hs,k}^{\min} \leq \tilde{E}_{hs,k,t} \leq E_{hs,k}^{\max}) \geq 1 - \varepsilon_{hs,t}^E \quad (54)$$

$$E_{hs,k,0} = E_{hs,k,NT} \quad (55)$$

where $\varepsilon_{\text{main},t}$, $\varepsilon_{eh,t}$, $\varepsilon_{hs,t}^{ch}$, $\varepsilon_{hs,t}^{dis}$, and $\varepsilon_{hs,t}^E$ are the predefined risk parameters.

3) *Network Constraints*: The network constraints include the total electrical power balance of the building clusters and the heat balance of individual buildings:

$$\tilde{P}_{\text{main},t} = \sum_{k \in \varphi_b} [P_{ac,k,t} + \tilde{P}_{eh,k,t} + \tilde{P}_{\text{load},k,t} - P_{pv,k,t}] \quad (56)$$

$$H_{pv,k,t} + \tilde{H}_{hs,k,t}^{dis} + \tilde{H}_{eh,k,t} = \tilde{H}_{hs,k,t}^{ch} + \tilde{H}_{\text{load},k,t} \quad (57)$$

Take (39), (40), (45)-(49) into (56) and (57), the constraints are reformulated as below:

$$\hat{P}_{\text{main},t} = \sum_{k \in \varphi_b} [P_{ac,k,t} + \hat{P}_{eh,k,t} + \hat{P}_{\text{load},k,t} - P_{pv,k,t}] \quad (58)$$

$$H_{pv,k,t} + \hat{H}_{hs,k,t}^{dis} + \hat{H}_{eh,k,t} = \hat{H}_{hs,k,t}^{ch} + \hat{H}_{\text{load},k,t} \quad (59)$$

C. Reformulate for DRCC Model

For ease of exposition, we consider a generic DR chance constraint as:

$$\mathbb{P} \{a_k^T x \leq b_k, k \in [K]\} \geq 1 - \varepsilon \quad (60)$$

By applying the Bonferroni approximation method [42] to handle (60), it is approximately transformed into (61).

$$\begin{cases} \mathbb{P} \{a_k^T x \leq b_k\} \geq 1 - \varepsilon_k, k \in [K] \\ \sum \varepsilon_k \leq \varepsilon, \varepsilon_k \geq 0 \end{cases} \quad (61)$$

We consider the conditional value at risk (CVaR) approximation for the nonconvex DR chance constraint that is a convex inner approximation [43]. Therefore, we have:

$$\begin{aligned} & \sup_{\mathbb{P} \in \mathcal{D}} \text{CVaR}_{\varepsilon_k} (a_k^T x \leq b_k) \leq 0 \\ & \Rightarrow \inf_{\mathbb{P} \in \mathcal{D}} \mathbb{P} (a_k^T x \leq b_k) \geq 1 - \varepsilon_k \\ & \Rightarrow \inf_{\beta \in \mathbb{R}} \left(\beta + \frac{1}{\varepsilon_k} \sup_{\mathbb{P} \in \mathcal{D}} \mathbb{E}_{\mathbb{P}} [a_k^T x - b_k - \beta]_+ \right) \leq 0 \end{aligned} \quad (62)$$

The CVaR constraint under the ambiguity set \mathcal{P}_W is equivalent to the following linear program [44]:

$$\min_{\beta, v, z_i} \left[\beta + \frac{1}{\varepsilon_k} \left(\theta v + \frac{1}{N} \sum_{i=1}^N z_i \right) \right] \leq 0 \quad (63)$$

$$\text{s.t. } a_k^T x - b_k - \beta \leq z_i, \forall i \in [N] \quad (64)$$

$$\|a\|_{\infty} \leq v \quad (65)$$

$$\beta \in \mathbb{R}, z_i \in \mathbb{R}_+, \forall i \in [N] \quad (66)$$

where β , v , and z_i are auxiliary variables.

D. Differential Linearization

To improve the solution efficiency, the differential linearization method is employed to transform the first-order differential equations to linearized constraints [12]. First, the first-order differential equations proposed can be converted into the following unified form:

$$C \frac{dT^{\chi_2}(t)}{dt} = R [T^{\chi_1} - T^{\chi_2}] + Q(t), t \in [0, NT] \quad (67)$$

where C is the equivalent heat capacity; R is the equivalent thermal resistance; $T^{\chi_2}(t)$ is the calculated temperature of the target layer at time t ; $T^{\chi_1}(t)$ is the temperature of layers associated with target layer; $[0, NT]$ is the optimization period.

Take $\Delta\tau = \frac{\Delta t}{N}$, for each time t_m in Δt can be described as follows:

$$\frac{dT^{\chi}(t_m)}{dt} = \frac{T^{\chi}(t_m + \Delta\tau) - T^{\chi}(t_m)}{\Delta\tau}, t_m \in [t_I, t_{II}] \quad (68)$$

Further, the computational procedure of $T^{\chi}(t_m)$ can be differential linearized as follows:

$$\begin{aligned} T^{\chi_2}(t_I + \Delta\tau) &= \frac{R\Delta\tau}{C} [T^{\chi_1}(t_I) - T^{\chi_2}(t_I)] \\ &+ \frac{\Delta\tau}{C} Q(t_I) + T^{\chi_2}(t_I) \\ &\dots \end{aligned}$$

$$\begin{aligned} T^{\chi_2}(t_m : t_I + m\Delta\tau) &= \frac{R\Delta\tau}{C} [T^{\chi_1}(t_I) - T^{\chi_2}(t_I + (m-1)\Delta\tau)] \\ &+ \frac{\Delta\tau}{C} Q(t_I) + T^{\chi_2}(t_I + (m-1)\Delta\tau) \end{aligned} \quad (69)$$

where $\Delta\tau$ is the calculation step; $\Delta t = t_{II} - t_I$ is the optimization step; N is the number of differentials.

VI. CASE STUDIES

In this section, two building clusters in Macao are performed to analyze the dynamic characteristics of building energy system with surrounding microclimate and verify the effectiveness of proposed optimal dispatch strategy. The selected areas are depicted in Fig. 4 (data from the Institute of Geographic Sciences and Natural Resources Research, CAS [45]), including the building cluster in University of Macau (58 individuals, building density 19%, building area 239,202m²) and building cluster in Macau Peninsula (141 individuals, building density 42%, building area 210,463m²). For each individual building,



Fig. 4. The building clusters in University of Macau (a) and Macau Peninsula (b).

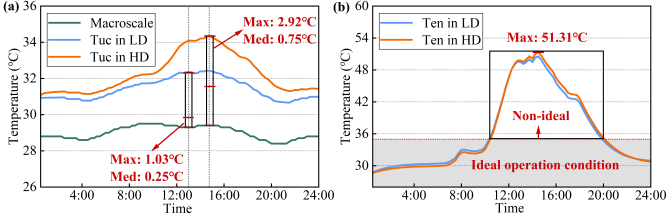


Fig. 5. Microclimate distribution in low-density (LD) and high-density (HD) building clusters: (a) Urban canopy layer temperature (T_{uc}); (b) Building envelop layer temperature (T_{en}).

it is assumed that 85% of the effective rooftop area is available for the installation of photovoltaic panels, and that air conditioning systems are installed in all selected buildings. After applying differential linearization and reformulating the distributionally robust chance-constrained model, the entire framework is transformed into a mixed-integer programming problem. The proposed optimization is calculated in MATLAB R2024a based on Yalmip toolbox by calling the CPLEX commercial solver, and the PC environment is Intel Xeon Gold 5118 CPU @ 2.30 GHz RAM 64 GB.

A. Dynamic Efficiency and User Demand with Surrounding Microclimate Interactions

1) *Microclimate Distribution:* Fig. 5 summarizes the differences in microclimate temperature distributions for two building clusters. It is evident that microclimate temperatures exceed those observed in macroscale meteorological data. In the high-density building cluster of the Macao Peninsula, urban canopy temperatures are elevated by more than 2.92°C , as shown in Fig. 5(a). Even in the low-density building cluster of the University of Macau, the temperature increase reaches a maximum of 1.03°C , with a median of 0.25°C . The primary factors driving this increase are the significant anthropogenic heat generated by human activities and the large number of man-made surfaces, which enhance solar radiation absorption. In high-density areas, building wind resistance exacerbates heat accumulation, further elevating urban temperatures. Additionally, compared to the urban canopy layer, the building envelope layer—typically composed of cement with low specific heat—heats up more rapidly after absorbing solar radiation, as shown in Fig. 5(b). At peak solar radiation, building envelope temperatures reach a maximum of

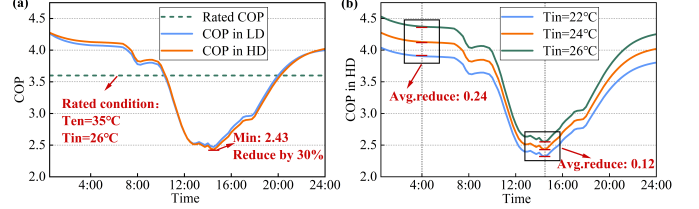


Fig. 6. The dynamic COP: (a) Under low-density (LD) and high-density (HD) building clusters; (b) Under different indoor set temperature (T_{in}).

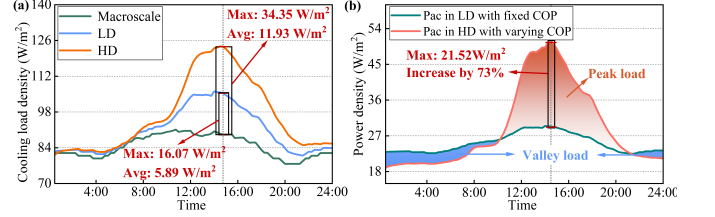


Fig. 7. The building load in low-density (LD) and high-density (HD) building clusters: (a) Cooling load; (b) Power demand of ACs (Pac).

51.31°C . Additionally, envelope temperatures exhibit minimal sensitivity to building density.

2) *Dynamic COP of ACs:* The COP of widely used air-cooled air conditioners is influenced by both indoor and outdoor operating conditions. Specifically, the air-conditioning condensing unit, located in the building envelope, typically operates in a non-ideal environment for most of the day, as shown in Fig. 5(b). Fig. 6 illustrates the variation in COP under microclimate conditions with different indoor set temperatures. First, under rated conditions (outdoor temperature of 35°C and indoor temperature of 26°C), the COP remains constant at 3.6. Conversely, considering the realistic conditions, the COP decreases to 2.43 as the outdoor temperature rises, a reduction of 30%. The primary reason has been shown in Fig. 1(d). During the air-conditioning refrigeration cycle, an increase in outdoor temperature raises the actual condensing temperature of ACs. At this time, to ensure the refrigerant is fully liquefied in the condenser, the compressor must consume more power to increase condensate pressure. Simultaneously, the higher condensate temperature reduces the cooling capacity of the evaporator, resulting in less cooling output. Furthermore, indoor set temperatures generally range from 22°C to 26°C , depending on user comfort. Fig. 6(b) shows how the COP varies with different indoor set temperatures. At the highest outdoor temperature, a 2°C deviation from the indoor set temperature results in an average COP loss of 0.12. Under rated operating conditions, average COP loss increases to 0.24.

3) *Dynamic Cooling Load:* Based on (43), the indoor cooling load demand is directly influenced by microclimate conditions, including solar radiation, urban canopy temperature, and building envelope temperature. Fig. 7(a) shows the cooling load density for building clusters with varying densities. It is evident that conventional calculations, which rely on macroscale meteorological parameters, tend to be overly conservative, with the cooling load density remaining below 90 W/m^2 . In contrast, the realistic microclimate conditions result in an average increase of 11.93 W/m^2 in high-density building

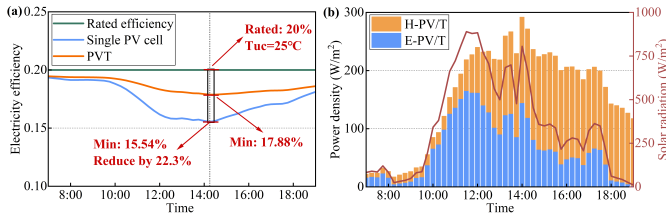


Fig. 8. PV/T operation characteristic: (a) Generation efficiency under different conditions; (b) Heat output (H-PV/T) and electricity output (E-PV/T).

blocks, with peak values exceeding 30 W/m^2 . Similarly, in low-density building blocks, the increase in cooling load density exceeds 17%. As discussed in the previous section, the rise in microclimate temperatures reduces the cooling efficiency of air conditioners. Consequently, the decrease in COP, combined with the increased cooling demand, leads to significant peak-to-valley variations, as shown in Fig. 7(b). The green line represents the AC power density in the low-density building cluster with ideal COP, while the red line represents the high-density cluster with the dynamic characteristic. The results show that, under microclimatic conditions, the peak air conditioning power density increases by more than 70%, reaching 21.52 W/m^2 , compared to the ideal condition. Furthermore, the daily peak-to-valley ratio (peak-to-valley/maximum load) reaches 61%.

4) Dynamic Efficiency of PV/T: The power generation efficiency of PV cells is strongly influenced by operating temperature. Under rated test conditions (25°C), the efficiency of PV panels is 20%, as shown in Fig. 8(a). In reality, the temperature of PV panels can rise significantly above the ideal value due to solar radiation absorption. Furthermore, under microclimatic conditions, the heat from the PV panels is not effectively dissipated. As a result, the peak temperature of the PV panels can exceed 50°C , causing the efficiency to drop to 15.54%. By incorporating a cooling circulation system, the PV/T employs a condensate to remove heat from the PV panels, transferring the waste heat to the condenser. This results in higher electricity generation efficiency compared to single PV panels, as shown in Fig. 8(a). Additionally, the PV/T system not only generates electricity but also produces hot water, as illustrated in Fig. 8(b). It can be observed that power generation fluctuates in direct correlation with solar radiation, while the output of hot water lags behind the PV panel temperature, primarily occurring between 13:00 and 17:00, with peak output reaching 160 W/m^2 .

B. The Effectiveness of Proposed Optimal Dispatch Strategy

The high-density building cluster in the Macau Peninsula is selected for detailed analysis. To efficiently construct ambiguity set, we utilize historical load data to generate an empirical distribution. A random set of 1,000 examples is then generated based on a Gaussian distribution, forming the data pool. Based on (41) and (42), the radius of the Wasserstein distance between the random and empirical distributions is set to $\lambda_{\max}(d_W)$. Four test scenarios are set to evaluate the effectiveness of the proposed model: Case 1: Ignoring microclimate

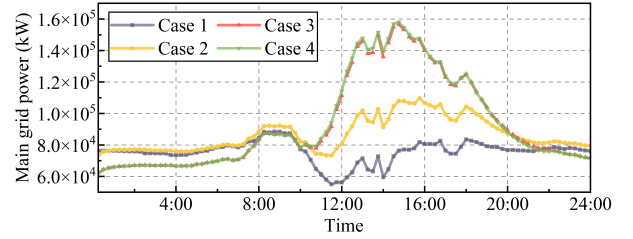


Fig. 9. Electricity purchased from main grid of building cluster in Case 1-4.

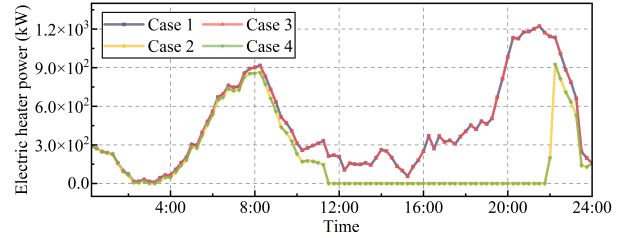


Fig. 10. The electric heater output of individual building in Case 1-4.

interaction and dynamic characteristics of facilities; Case 2: Considering microclimate interaction as well as the dynamic characteristics of the PV/T; Case 3: Considering microclimate interaction as well as the dynamic characteristics of ACs; Case 4: Considering microclimate interaction and dynamic characteristics of facilities.

1) Dispatch Result Analysis: Fig. 9 illustrates the total amount of purchased electricity for the building clusters across Cases 1-4. It is apparent that Case 1 significantly underestimates the actual energy demand of the building cluster due to ignoring real operating conditions. Specifically, comparing Case 1 and Case 2 in the periods of 12:00 to 16:00, it is evident that the microclimate interactions lead to a peak load increase of over 50%. More critically, comparing Case 1 with Case 3, the combination of microclimate effects and facility energy efficiency reduction nearly doubles the peak load. This can be attributed to two key factors: first, the increase in microclimate temperature leads to a rapid rise in the building's cooling load demand; and second, both the cooling capacity of ACs and the power generation capacity of PV/T are significantly reduced during the midday high-temperature period. Additionally, the two main grid power curves in Case 3 and Case 4 are similar, indicating that the PV/T heat output has minimal impact on total energy consumption. This result is primarily driven by the fact that the selected building

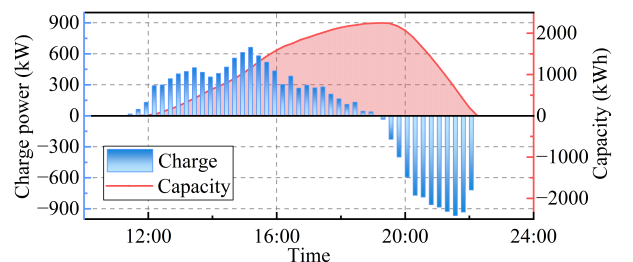


Fig. 11. The operation state of hot water tank of individual building in Case4.

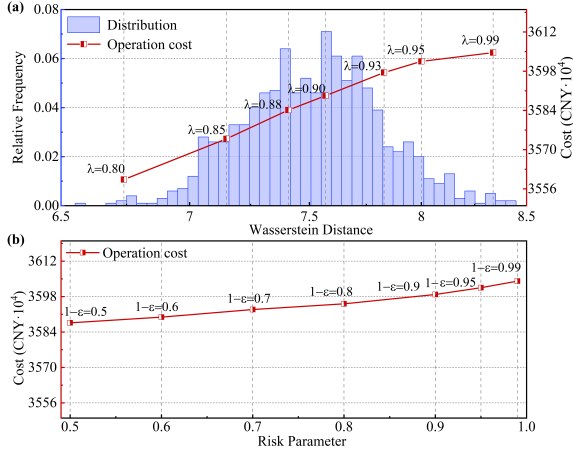


Fig. 12. Operation cost under different radius (a) and risk parameters (b).

cluster in the Macau Peninsula consists mainly of high-rise, high-density office buildings, where heat loads account for a small proportion of overall energy consumption. To further investigate the dispatch strategy for heat loads, we analyze the results for an individual building, as shown in Fig. 10 and Fig. 11. First, when the dynamic characteristics of the PV/T system are ignored, the output of the electric heater closely follows the heat load profile observed in Case 1 and Case 3. In reality, a substantial amount of waste heat could be utilized to meet the hot water demand of users through the PV/T evaporator in conjunction with the condenser. Notably, in the periods of 12:00 to 17:00, the operation of the electric heater shutdown (Fig. 10), while excess waste heat is effectively stored in the water tank. From 18:30 to 22:00, the water tank continues to supply heat, meeting the building users' demand and significantly reducing the electricity consumption of the electric heater.

2) *The Sensitivity Analysis of DRCC:* The Wasserstein-distance-based DRCC shows sensitivity to both ambiguity set radius and risk parameters, as shown in Fig. 12. First, Fig. 12(a) shows the distribution of the Wasserstein distance between all random and empirical distributions, which is approximated as a normal distribution. When the radius parameter λ is greater than 0.95, the uncertainty set will expand to include low-probability extreme scenarios. At this time, the system requires more reserves to address potential extremes. In contrast, when λ is less than 0.85, the uncertainty set narrows, leading to an overly optimistic optimization result and increasing the risk of exceeding the limits of the actual scenario. Besides, it is evident that the system's operating cost decreases significantly with smaller values of λ . Fig. 12(b) examines the impact of the risk parameter ε on the dispatch strategy. The risk parameter reflects the system's tolerance to uncertainty: a small risk parameter forces the system to adopt a more conservative strategy to handle the worst-case scenarios. Conversely, a high risk parameter allows the system to violate constraints in certain scenarios, potentially leading to less reliable operation but a reduction in cost. Comparing Fig. 12(a) and Fig. 12(b), it is apparent that the operating cost is more sensitive to changes in the ambiguity set radius than

to the risk parameter.

VII. CONCLUSION AND DISCUSSION

In this paper, we propose a microclimate-interactive energy management framework for building clusters, particularly focusing on terminal-level energy dynamics and user demand under urban-scale microclimate feedback. First, the urban-scale microclimate formation model is proposed to incorporate underlying structures and anthropogenic emissions. Then, the terminal-level dynamic energy efficiency model is proposed to build numerical relationship between energy facilities and surrounding microclimate. Furthermore, the distributionally robust chance-constrained optimization method is employed to address user-demand uncertainty. Finally, the numerical analysis on building clusters in Macao demonstrates that: (i) Microclimate conditions vary with building energy activities and underlying structure changes, leading to temperature differences of more than 1.8°C between high- and low-density building clusters; (ii) Building energy activities are highly sensitive to microclimate conditions, with both ACs and PV/T experience a more than 20% reduction in energy efficiency, while cooling demand more than doubles; (iii) The DRCC optimization strategy effectively addresses load uncertainty and exhibits sensitivity to ambiguity sets and risk parameters.

However, it is important to note that this study still has some limitations due to certain simplifications and assumptions. First, the scope of the model is confined to building clusters within urban areas, neglecting the impact of urban boundaries and surrounding oceans. Second, the dynamic facility models are based on generic typical device structures and parameters, without accounting for the differences in materials and processes across different brands. Lastly, it is assumed that each building within the cluster has an energy manager with the authority to access data and control the operations of individual buildings.

Based on the analysis presented in this paper, we have identified significant interactions between building energy activities and the surrounding microclimate. Our future work will focus on the following areas: (i) The challenges posed by ongoing climate change to the safe and reliable operation of building energy systems, particularly across different typical climate zones globally; (ii) The development of effective market mechanisms and pricing strategies to facilitate the coordinated optimization of building energy activities and the environment; (iii) The implementation of robust privacy protection and data handling mechanisms to enhance the adaptability and scalability of the model's applications.

REFERENCES

- [1] IEA, “Tracking clean energy progress 2023,” URL <https://www.iea.org/reports/tracking-clean-energy-progress-2023>.
- [2] S. Joshi, S. Mittal, P. Holloway, P. R. Shukla, B. Ó Gallachóir, and J. Glynn, “High resolution global spatiotemporal assessment of rooftop solar photovoltaics potential for renewable electricity generation,” *Nature communications*, vol. 12, no. 1, pp. 1–15, 2021.
- [3] X. Sheng, S. Lin, W. Liang, Y. Pan, and M. Liu, “Interval economic dispatch for commercial campus integrated energy system with demand response considering multiple uncertainties,” *CSEE Journal of Power and Energy Systems*, vol. 11, no. 3, pp. 1297–1311, 2025.

- [4] Z. Ji, X. Liu, and D. Tang, "Game-theoretic applications for decision-making behavior on the energy demand side: a systematic review," *Protection and Control of Modern Power Systems*, vol. 9, no. 2, pp. 1–20, 2024.
- [5] T. Qi, H. Hui, and Y. Song, "Exploring the feasible regulation region of building hvac systems within hydro-thermal comfort," *IEEE Transactions on Smart Grid*, vol. 16, no. 4, pp. 2926–2939, 2025.
- [6] Z. Zhang, H. Hui, and Y. Song, "Mitigating the vicious cycle between urban heatwaves and building energy systems in guangdong-hong kong-macao greater bay area," *The Innovation Energy*, vol. 2, no. 2, pp. 100080–1, 2025.
- [7] A. M. Elbreki, M. Alghoul, A. Al-Shamani, A. Ammar, B. Yegani, A. M. Aboghrara, M. Rusaln, and K. Sopian, "The role of climatic-design-operational parameters on combined pv/t collector performance: A critical review," *Renewable and Sustainable Energy Reviews*, vol. 57, pp. 602–647, 2016.
- [8] E. M. Barreira, C. O. Negrão, and C. J. Hermes, "Thermoeconomic analysis and optimization of residential split-type air conditioners," *Applied Thermal Engineering*, vol. 50, no. 1, pp. 629–636, 2013.
- [9] S. Qian, J. Ling, Y. Hwang, R. Radermacher, and I. Takeuchi, "Thermodynamics cycle analysis and numerical modeling of thermoelastic cooling systems," *International Journal of Refrigeration*, vol. 56, pp. 65–80, 2015.
- [10] J. Yu, D. Yang, J. Cao, P. Dehghanian, and N. Tomin, "Robust state estimation for an electricity-gas-heat integrated energy system considering dynamic characteristics," *Protection and Control of Modern Power Systems*, vol. 9, no. 1, pp. 65–80, 2024.
- [11] B. Hu, X. Cheng, C. Shao, T. Niu, C. Li, Y. Sun, W. Huang, and K. Xie, "Model and data hybrid driven approach for quantifying the meteorology-dependent demand flexibility of building thermal loads," *CSEE Journal of Power and Energy Systems*, vol. 11, no. 1, pp. 394–405, 2025.
- [12] Z. Zhang, H. Hui, and Y. Song, "Response capacity allocation of air conditioners for peak-valley regulation considering interaction with surrounding microclimate," *IEEE Transactions on Smart Grid*, vol. 16, no. 2, pp. 1155–1167, 2025.
- [13] L. Zhao, X. Lee, R. B. Smith, and K. Oleson, "Strong contributions of local background climate to urban heat islands," *Nature*, vol. 511, no. 7508, pp. 216–219, 2014.
- [14] Y. Sun, X. Zhang, G. Ren, F. W. Zwiers, and T. Hu, "Contribution of urbanization to warming in china," *Nature Climate Change*, vol. 6, no. 7, pp. 706–709, 2016.
- [15] Y. Kikegawa, Y. Genchi, H. Kondo, and K. Hanaki, "Impacts of city-block-scale countermeasures against urban heat-island phenomena upon a building's energy-consumption for air-conditioning," *Applied Energy*, vol. 83, no. 6, pp. 649–668, 2006.
- [16] M. Santamouris, "Recent progress on urban overheating and heat island research. integrated assessment of the energy, environmental, vulnerability and health impact. synergies with the global climate change," *Energy and Buildings*, vol. 207, p. 109482, 2020.
- [17] K. Javanroodi, V. M. Nik, M. G. Giometto, and J.-L. Scartezzini, "Combining computational fluid dynamics and neural networks to characterize microclimate extremes: Learning the complex interactions between meso-climate and urban morphology," *Science of The Total Environment*, vol. 829, p. 154223, 2022.
- [18] X. Yang, Y. Li, Z. Luo, and P. W. Chan, "The urban cool island phenomenon in a high-rise high-density city and its mechanisms," *International Journal of Climatology*, vol. 37, no. 2, pp. 890–904, 2017.
- [19] M. Martin, A. Afshari, P. R. Armstrong, and L. K. Norford, "Estimation of urban temperature and humidity using a lumped parameter model coupled with an energyplus model," *Energy and Buildings*, vol. 96, pp. 221–235, 2015.
- [20] S. Duan, Z. Luo, X. Yang, and Y. Li, "The impact of building operations on urban heat/cool islands under urban densification: A comparison between naturally-ventilated and air-conditioned buildings," *Applied Energy*, vol. 235, pp. 129–138, 2019.
- [21] A. Shahsavari and M. Akbari, "Potential of solar energy in developing countries for reducing energy-related emissions," *Renewable and Sustainable Energy Reviews*, vol. 90, pp. 275–291, 2018.
- [22] C. Şirin, J. Goggins, and M. Hajdukiewicz, "A review on building-integrated photovoltaic/thermal systems for green buildings," *Applied Thermal Engineering*, vol. 229, p. 120607, 2023.
- [23] X. Li, K. Xie, C. Shao, B. Hu, W. Huang, C. Pan, and X. Du, "A sensitivity-based rolling operational reliability evaluation method following the changing available generation capacity of renewable energies," *IEEE Transactions on Power Systems*, vol. 40, no. 1, pp. 166–177, 2025.
- [24] C. Zhang, L. Chen, Z. Zhou, Z. Wang, L. Wang, and W. Wei, "Heat harvesting characteristics of building façades integrated photovoltaic/thermal-heat pump system in winter," *Renewable Energy*, vol. 215, p. 118909, 2023.
- [25] D. A. E. Chekired, S. Dhaou, L. Khoukhi, and H. T. Mouftah, "Dynamic pricing model for ev charging-discharging service based on cloud computing scheduling," in *2017 13th International Wireless Communications and Mobile Computing Conference (IWCMC)*, pp. 1010–1015, IEEE, 2017.
- [26] D. Said, "Intelligent photovoltaic power forecasting methods for a sustainable electricity market of smart micro-grid," *IEEE Communications Magazine*, vol. 59, no. 7, pp. 122–128, 2021.
- [27] IEA, "Space cooling," URL <https://www.iea.org/reports/space-cooling-2>, 2023.
- [28] Y. Zhang, Q. Ai, and Z. Li, "Intelligent demand response resource trading using deep reinforcement learning," *CSEE Journal of Power and Energy Systems*, vol. 10, no. 6, pp. 2621–2630, 2024.
- [29] P. Yu, H. Zhang, Y. Song, H. Hui, and C. Huang, "Frequency regulation capacity offering of district cooling system: An intrinsic-motivated reinforcement learning method," *IEEE Transactions on Smart Grid*, vol. 14, no. 4, pp. 2762–2773, 2023.
- [30] P. Martínez, J. Ruiz, C. Cutillas, P. Martínez, and A. Kaiser, "Experimental study on energy performance of a split air-conditioner by using variable thickness evaporative cooling pads coupled to the condenser," *Applied Thermal Engineering*, vol. 105, pp. 1041–1050, 2016.
- [31] S. Nada and M. Said, "Performance and energy consumptions of split type air conditioning units for different arrangements of outdoor units in confined building shafts," *Applied Thermal Engineering*, vol. 123, pp. 874–890, 2017.
- [32] P. Yu, H. Zhang, Y. Song, Z. Wang, H. Dong, and L. Ji, "Safe reinforcement learning for power system control: A review," *Renewable and Sustainable Energy Reviews*, vol. 223, p. 116022, 2025.
- [33] Y. Tian, Z. Li, W. Wu, and M. Fan, "Joint chance-constrained economic dispatch involving joint optimization of frequency-related inverter control and regulation reserve allocation," *CSEE Journal of Power and Energy Systems*, vol. 11, no. 3, pp. 1030–1044, 2025.
- [34] R. Xie, P. Pinson, Y. Xu, and Y. Chen, "Robust generation dispatch with purchase of renewable power and load predictions," *IEEE Transactions on Sustainable Energy*, vol. 15, no. 3, pp. 1486–1501, 2024.
- [35] I. Khabbouchi, D. Said, A. Oukaira, I. Mellal, and L. Khoukhi, "Machine learning and game-theoretic model for advanced wind energy management protocol (AWEMP)," *Energies*, vol. 16, no. 5, p. 2179, 2023.
- [36] X. Xu, Y. Gao, H. Wang, Z. Yan, M. Shahidehpour, and Z. Tan, "Distributionally robust optimization of photovoltaic power with lifted linear decision rule for distribution system voltage regulation," *IEEE Transactions on Sustainable Energy*, vol. 15, no. 2, pp. 758–772, 2024.
- [37] H. Li, Q. Wu, L. Yang, H. Zhang, and S. Jiang, "Distributionally robust negative-emission optimal energy scheduling for off-grid integrated electricity-heat microgrid," *IEEE Transactions on Sustainable Energy*, vol. 15, no. 2, pp. 803–818, 2024.
- [38] L. Yang, H. Li, H. Zhang, Q. Wu, and X. Cao, "Stochastic-distributionally robust frequency-constrained optimal planning for an isolated microgrid," *IEEE Transactions on Sustainable Energy*, vol. 15, no. 4, pp. 2155–2169, 2024.
- [39] Q. Hou, G. Chen, N. Dai, and H. Zhang, "Distributionally robust chance-constrained optimization for soft open points operation in active distribution networks," *CSEE Journal of Power and Energy Systems*, vol. 11, no. 2, pp. 637–648, 2025.
- [40] N. Centre, "Ground-based basic meteorological observations in china," URL <http://data.cma.cn/>, 2020.
- [41] P. Mohajerin Esfahani and D. Kuhn, "Data-driven distributionally robust optimization using the wasserstein metric: Performance guarantees and tractable reformulations," *Mathematical Programming*, vol. 171, no. 1, pp. 115–166, 2018.
- [42] X. Geng and L. Xie, "Data-driven decision making in power systems with probabilistic guarantees: Theory and applications of chance-constrained optimization," *Annual reviews in control*, vol. 47, pp. 341–363, 2019.
- [43] S. Zymler, D. Kuhn, and B. Rustem, "Distributionally robust joint chance constraints with second-order moment information," *Mathematical Programming*, vol. 137, pp. 167–198, 2013.
- [44] Z. Chen, D. Kuhn, and W. Wiesemann, "Data-driven chance constrained programs over wasserstein balls," *Operations Research*, vol. 72, no. 1, pp. 410–424, 2024.
- [45] I. of Geographic Sciences and C. Natural Resources Research, "Resource and environment science and data center," URL <https://www.resdc.cn/data.aspx?DATAID=270>, 2020.



Zhenwei Zhang (Graduate Student Member, IEEE) received the M.S. degrees in Electrical Engineering from Shandong University, Jinan, China, in 2022.

Now, he is pursuing the Ph.D. degree in Electrical and Computer Engineering at University of Macau, Macao SAR, China. His research focuses on the coupling between urban microclimate and urban energy system, demand-side resources management, optimal operation of integrated energy system.



Hongxun Hui (Senior Member, IEEE, Senior Member, CSEE) received the B.E. and Ph.D. degrees in electrical engineering from Zhejiang University, Hangzhou, China, in 2015 and 2020, respectively.

From 2018 to 2019, he was a visiting scholar with the Advanced Research Institute, Virginia Tech, and the CURENT Center, University of Tennessee. He is currently an Assistant Professor with the State Key Laboratory of Internet of Things for Smart City, University of Macau, Macao SAR, China. His research interests include optimization and control

of power system, demand response, and Internet of Things technologies for smart energy.



Yonghua Song (Fellow, IEEE, Fellow, CSEE) received the B.E. degree from Chengdu University of Science and Technology, Chengdu, China, in 1984, and the Ph.D. degree from China Electric Power Research Institute, Beijing, China, in 1989, both in electrical engineering.

From 1989 to 1991, he was a Postdoctoral Fellow with Tsinghua University, Beijing, China. He then held various positions with Bristol University, Bristol, U.K.; Bath University, Bath, U.K.; John Moores University, Liverpool, U.K., from 1991 to 1996. In 1997, he was a Professor of Power Systems with Brunel University, where he has been a Pro-Vice Chancellor for Graduate Studies since 2004. In 2007, he took up a Pro-Vice Chancellorship and Professorship of Electrical Engineering with the University of Liverpool, Liverpool. In 2009, he was with Tsinghua University as a Professor of Electrical Engineering and an Assistant President and the Deputy Director with the Laboratory of Low-Carbon Energy. During 2012 to 2017, he was the Executive Vice President with Zhejiang University, as well as Founding Dean of the International Campus and Professor of Electrical Engineering and Higher Education of the University. Since 2018, he has been Rector of the University of Macau and the Director with the State Key Laboratory of Internet of Things for Smart City. His current research interests include smart grid, electricity economics, and operation and control of power systems.

Dr. Song was elected as the Vice-President of Chinese Society for Electrical Engineering (CSEE) and appointed as the Chairman of the International Affairs Committee of the CSEE in 2009. In 2004, he was elected as a Fellow of the Royal Academy of Engineering, U.K. In 2019, he was elected as a Foreign Member of the Academia Europaea. He was the recipient of D.Sc. by Brunel University in 2002, Honorary D.Eng. by the University of Bath in 2014, and Honorary D.Sc. by the University of Edinburgh in 2019.